

Diffraction at GaAs/Fe₃Si core/shell nanowires: The formation of nanofacets

B. Jenichen, M. Hanke, M. Hilse, J. Herfort, A. Trampert, and S. C. Erwin

Citation: *AIP Advances* **6**, 055108 (2016);

View online: <https://doi.org/10.1063/1.4949009>

View Table of Contents: <http://aip.scitation.org/toc/adv/6/5>

Published by the [American Institute of Physics](#)

Articles you may be interested in

[Magnetic properties of GaAs-Fe₃Si core-shell nanowires—A comparison of ensemble and single nanowire investigation](#)

AIP Advances **7**, 056305 (2017); 10.1063/1.4973748

[Epitaxial growth of Fe₃Si/GaAs\(001\) hybrid structures](#)

Applied Physics Letters **83**, 3912 (2003); 10.1063/1.1625426

[Electronic analog of the electro-optic modulator](#)

Applied Physics Letters **56**, 665 (1998); 10.1063/1.102730

[Strain dynamics during La₂O₃/Lu₂O₃ superlattice and alloy formation](#)

Journal of Applied Physics **119**, 215301 (2016); 10.1063/1.4950875

[Deep-level defects related to the emissive pits in thick InGaN films on GaN template and bulk substrates](#)

APL Materials **5**, 016105 (2017); 10.1063/1.4974935

[Growth of Fe₃Si/Ge/Fe₃Si trilayers on GaAs\(001\) using solid-phase epitaxy](#)

Applied Physics Letters **110**, 102103 (2017); 10.1063/1.4977833

HAVE YOU HEARD?

Employers hiring scientists and
engineers trust

PHYSICS TODAY | JOBS

www.physicstoday.org/jobs



Diffraction at GaAs/Fe₃Si core/shell nanowires: The formation of nanofacets

B. Jenichen,^{1,a} M. Hanke,¹ M. Hilse,¹ J. Herfort,¹ A. Trampert,¹
and S. C. Erwin²

¹*Paul-Drude-Institut für Festkörperelektronik, Hausvogteiplatz 5–7,
D-10117 Berlin, Germany*

²*Center for Computational Materials Science, Naval Research Laboratory, Washington DC,
20375, USA*

(Received 31 March 2016; accepted 28 April 2016; published online 5 May 2016)

GaAs/Fe₃Si core/shell nanowire structures were fabricated by molecular-beam epitaxy on oxidized Si(111) substrates and investigated by synchrotron x-ray diffraction. The surfaces of the Fe₃Si shells exhibit nanofacets. These facets consist of well pronounced Fe₃Si{111} planes. Density functional theory reveals that the Si-terminated Fe₃Si{111} surface has the lowest energy in agreement with the experimental findings. We can analyze the x-ray diffuse scattering and diffraction of the ensemble of nanowires avoiding the signal of the substrate and poly-crystalline films located between the wires. Fe₃Si nanofacets cause streaks in the x-ray reciprocal space map rotated by an azimuthal angle of 30° compared with those of bare GaAs nanowires. In the corresponding TEM micrograph the facets are revealed only if the incident electron beam is oriented along [110] in accordance with the x-ray results. Additional maxima in the x-ray scans indicate the onset of chemical reactions between Fe₃Si shells and GaAs cores occurring at increased growth temperatures. © 2016 Author(s). All article content, except where otherwise noted, is licensed under a Creative Commons Attribution (CC BY) license (<http://creativecommons.org/licenses/by/4.0/>). [<http://dx.doi.org/10.1063/1.4949009>]

I. INTRODUCTION

Semiconductor/ferromagnet core/shell nanowires (NWs) have gained a lot of interest recently.^{1–8} The cylindrical shape of the ferromagnet in such core/shell NWs causes a magnetization along the wire axis, i.e. perpendicular to the substrate surface.⁷ The lattice matching of the binary Heusler alloy Fe₃Si and GaAs is a prerequisite for defect-free molecular beam epitaxy (MBE) of high quality hybrid structures.^{9–13} So we have chosen to grow GaAs/Fe₃Si core/shell nanowire structures.⁷

The nucleation of a film on a planar substrate as well as on a core NW surface can be considered in a similar manner as wetting or nonwetting of liquids.¹⁴ If the film wets the substrate it will grow layer-by-layer in Frank van der Merwe growth mode. In this case the surface of the film is simply repeating the shape of the substrate. In the non-wetting case three-dimensional (3D) islands will form in the Volmer-Weber (VW) growth mode, similar to liquid droplets. Although Fe₃Si is lattice matched to GaAs it is not wetting the GaAs surface during growth, and we observed the strain-free VW island growth mode of Fe₃Si on GaAs.¹⁵ Thus Fe₃Si islands grow initially isolated and can adopt their equilibrium shape before coalescence. New facets may arise in such a way.

For the Ga-assisted catalyst-free growth of our GaAs-core NWs by MBE in the [111] direction only the {110} sidewalls are present for geometrical reasons, as the growth rate of the NWs along

^aElectronic mail: bernd.jenichen@pdi-berlin.de

[111] is dominating.¹⁶ In general during heteroepitaxial growth the GaAs in an As-rich environment could also adopt an equilibrium crystal shape consisting of {111}, {110} and {100} facets.¹⁷

Several examples for the formation of facets on isolated heteroepitaxial islands can be found in the literature. MBE grown GaAs/AlAs core/shell NWs were decorated by Stranski Krastanov (SK) growth of InAs islands.¹⁸ These islands exhibit {111} and {115} facets and develop preferentially at the <112>-oriented corners of the NWs. Ge islands on Si NWs exhibited {111}, {110} and {113} facets as a result of a SK growth process.¹⁹ Similarly small particles of Au on a MgO substrate adopt the equilibrium shape with {111} and {100} facets.²⁰

So in our system Fe₃Si/GaAs we can expect a strain-free VW island growth of Fe₃Si on GaAs{110}.¹⁵ The properties of the NWs are determined by the growth temperature T_S of the Fe₃Si.²¹ For certain growth temperatures a coincidence of the core- and shell-orientations was observed by high-resolution transmission electron microscopy (HRTEM) and selected area diffraction (SAD).⁸ Here the Fe₃Si growth was pseudomorphic on GaAs and the formation of facets at the Fe₃Si shell surface was detected as well. During TEM observations only a relatively small sample volume is probed. It seems reasonable to complement TEM measurements by an experiment that averages over many NWs. In this work, we investigate the Fe₃Si shells grown at different substrate temperatures T_S and characterize the facets using X-ray diffraction (XRD) in grazing incidence geometry, and scanning electron microscopy (SEM), together with HRTEM. With XRD we are facing the challenge to distinguish the signals of the proper core/shell NWs and the so-called parasitic metallic film which is unintentionally deposited between the NWs. The solution is the application of grazing incidence diffraction (GID) at zero incidence angle. In that way we can substantially reduce the signals of the substrate and the parasitic layer.

On the other hand in the present work we give a theoretical foundation to explain the experimental observations using density functional theory (DFT). We compare the energies of the different surfaces of the Fe₃Si shells.

II. THEORETICAL SECTION

The equilibrium state of the Fe₃Si surface as a function of composition is determined by the minimization of the grand potential Ω ,^{22,23} where E is the energy of the crystal, S and T are the entropy and the temperature of the system, n_i and μ_i are the numbers of atoms of sort i and the corresponding chemical potentials.

$$\Omega = E - TS - \sum n_i \mu_i, \quad (1)$$

This minimization is usually performed for the temperature $T = 0$. In other words the stability of the surface (i.e. its crystallographic orientation and its surface termination or chemical configuration) is given by its surface energy per unit area γ , which is a free energy expressed with respect to the chemical potentials μ_i , which represent reservoirs of the chemical species involved. This means:

$$\gamma \cdot A = E_t - n_{Fe} \mu_{Fe} - n_{Si} \mu_{Si}, \quad (2)$$

where A is the area of the surface unit cell, E_t is its total energy, and n_{Fe} and n_{Si} are the numbers of Fe and Si atoms in the cell. We assume the surface to be in thermodynamic equilibrium with the bulk material. This implies that $3\mu_{Fe} + \mu_{Si} = g_{Fe_3Si}$, the energy per formula unit of bulk Fe₃Si.^{24,25} This constraint implies that g can be expressed as a function of just one independent variable e.g. μ_{Si} . On the other hand the individual atomic chemical potentials can never exceed the energy of the condensed pure element, i.e. the energy per atom in bulk Fe and bulk Si. The three constraints jointly place an upper and lower limit on μ_{Si} . DFT²⁶⁻³⁰ in the generalized gradient approximation³¹ was applied in order to determine the surface energy of low index surfaces using the Vienna Ab Initio Simulation Package (VASP).^{32,33} The calculations were performed in a slab geometry using slabs from 12 to 16 Å thick and a vacuum region of 10 Å. All atomic positions were relaxed except the innermost 3-4 layers, until the largest force component on every atom was below 0.05 eV Å⁻¹. All of the calculations assumed a fully ordered ferromagnetic Fe₃Si lattice.

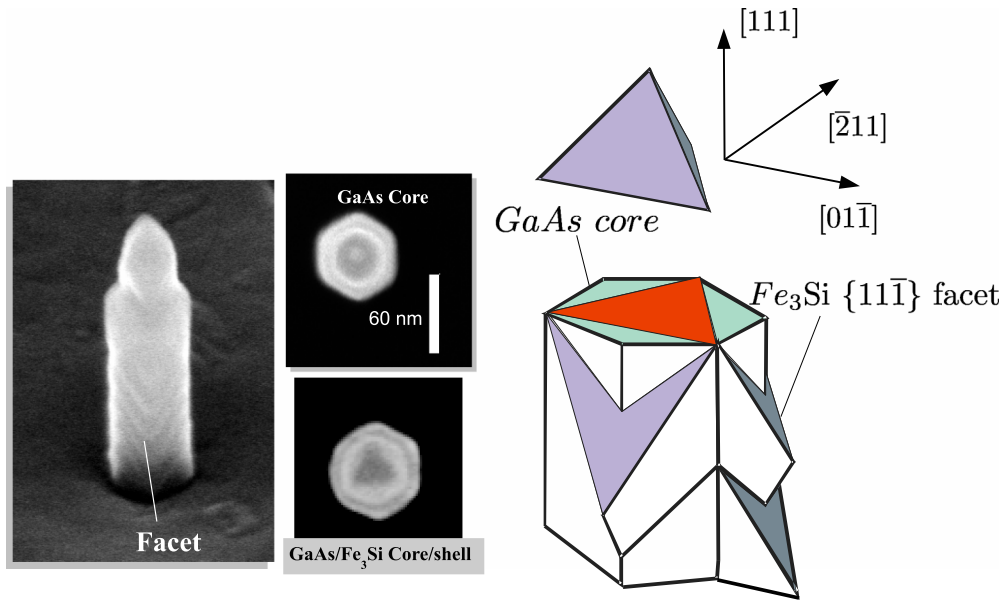


FIG. 1. (color online) SEM side view of a core/shell NW (left side) and SEM top views of a core and core/shell NWs (center) grown at $T_S = 200$ °C. A sketch of the GaAs core and the Fe_3Si shells (right side) with tilted $\{11\bar{1}\}$ facets is illustrating schematically the orientation relationship between the cores and the facets. In addition a tetrahedron consisting of $\{111\}$ planes is given.

III. EXPERIMENTAL SECTION

GaAs/ Fe_3Si core/shell NW structures were grown by MBE on Si(111) substrates.^{7,8} The resulting NW structures were investigated by X-ray diffraction, SEM, and TEM. The X-ray experiments were performed in grazing incidence geometry at the beamline BM 02 of the European Synchrotron Radiation Facility (ESRF) in Grenoble. The energy of the beam was 10 keV and the detector was an area detector S70 from Imxpad. The detector size is 560×120 pixels of size $130 \times 130 \mu m^2$ each. In order to minimize the penetration depth into substrate and parasitic film between the NWs a very

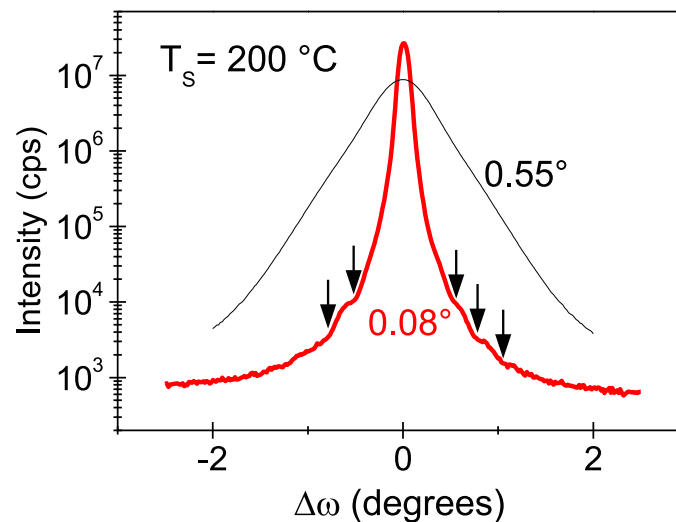


FIG. 2. XRD curve of the $(\bar{2}20)$ reflection of GaAs/ Fe_3Si core/shell NWs, $T_S = 200$ °C. A radial $\omega/2\theta$ -scan (thick red line) along the $[\bar{1}10]$ direction and an angular ω -scan perpendicular to the $[\bar{1}10]$ direction (thin black line), together with their full widths at half maximum (FWHM) are given. Thickness fringes are marked by arrows.

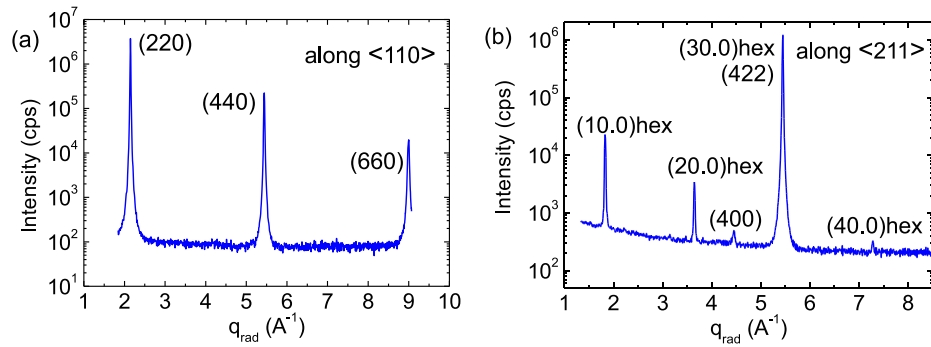


FIG. 3. XRD curves of the $\bar{2}20$ reflection of GaAs/Fe₃Si core/shell NWs. Radial XRD $\omega/2\theta$ -scans along $\langle 110 \rangle$ (a) and $\langle 211 \rangle$ (b).

small angle of incidence of 0.04° was chosen.³⁴ In this way the signal of the ensemble of NWs was always dominating the diffraction pattern. This was checked by observation of the vanishing signal of the single-crystal Si substrate, which would dominate the diffraction curve at larger angles of incidence. The TEM specimens are prepared as described in Ref. 8.

IV. RESULTS AND DISCUSSION

An area density of well oriented NWs of $\sim 5 \times 10^8 \text{ cm}^{-2}$ is found by SEM. In Fig. 1 SEM top views of a GaAs core NW and a GaAs/Fe₃Si core/shell NW ($T_S = 200^\circ\text{C}$) are given together with

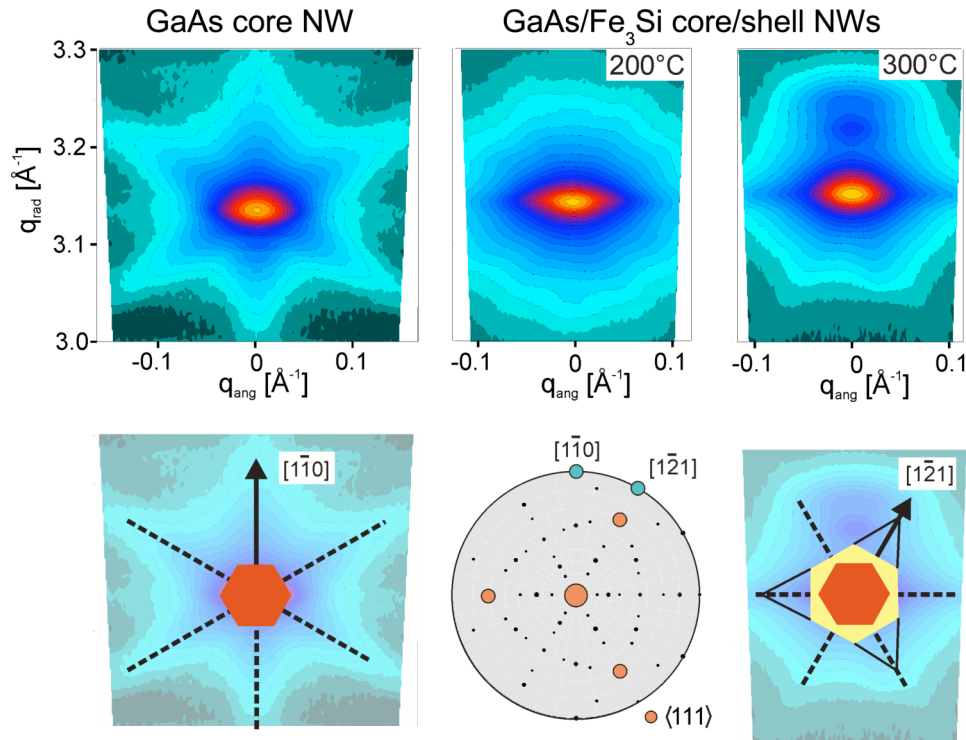


FIG. 4. $\bar{2}20$ in-plane reciprocal space maps of $[111]$ -oriented GaAs NWs (upper left) and GaAs/Fe₃Si core/shell NWs (upper center and upper right) grown by molecular beam epitaxy on Si(111). The growth temperatures of the Fe₃Si shells are given above. The crystallographic directions together with the corresponding sidewalls are sketched below. In the symbolic stereogram (middle) the $[1\bar{1}0]$ and $[1\bar{2}1]$ directions are marked by blue circles and the different $\{111\}$ directions by red circles. The radial direction of the scans is drawn vertically and the angular direction is directed horizontally in the figure.

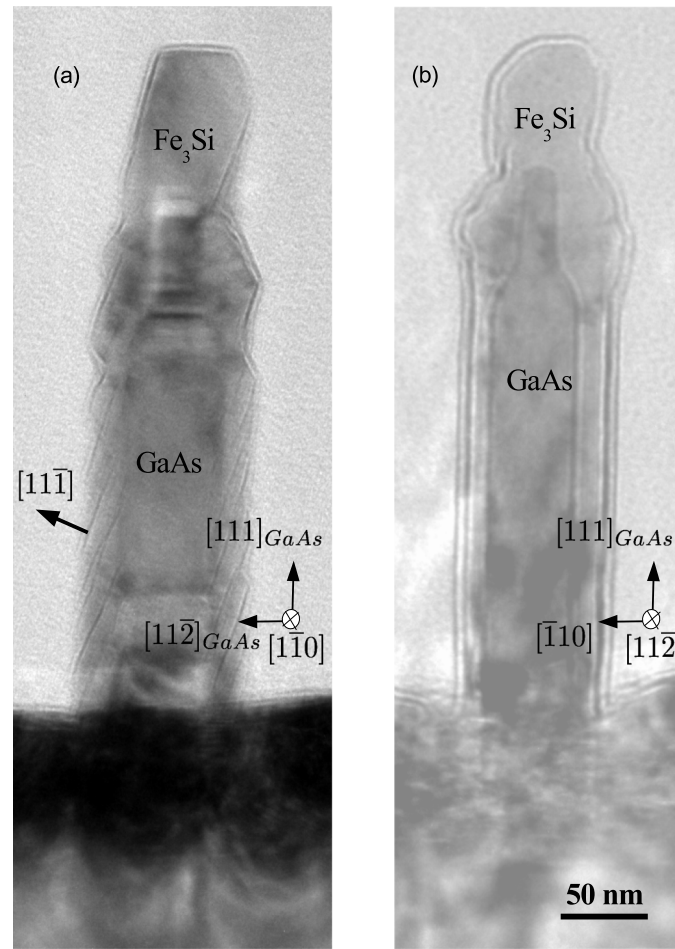
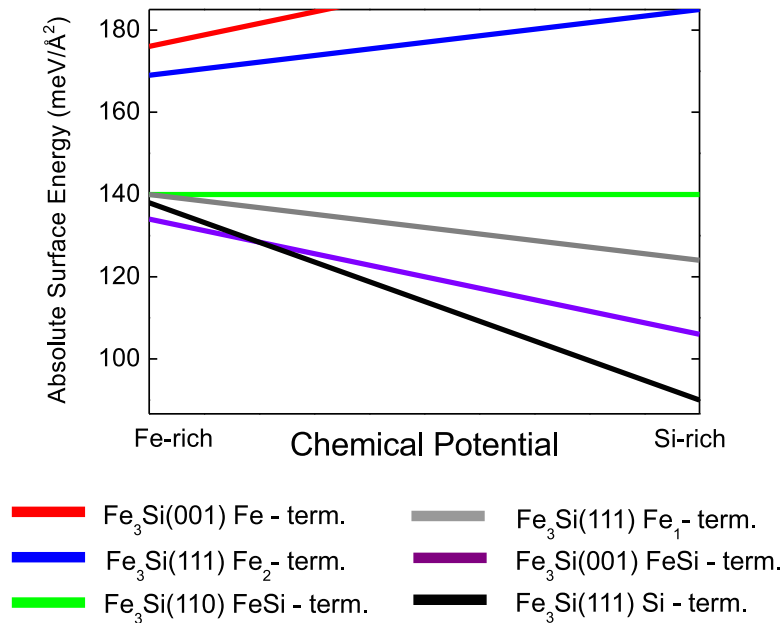


FIG. 5. Multi-beam bright-field TEM micrographs illustrating the orientations of the Fe_3Si shell facets with respect to the GaAs cores. The cores and shells are distinguished clearly. For the $[1\bar{1}0]$ direction of the electron beam (a) we see facets corresponding to tilted $\{11\bar{1}\}$ planes as sketched in Fig. 1. When the electron beam is running along the $[11\bar{2}]$ direction no facets are observed (b). The images are slightly defocused in order to increase the contrast of the surfaces and interfaces.

a side-view of a core/shell NW. Regular step patterns, facets, are clearly visible on the sidewalls of the NW. At the top of the NW a thinner part is visible. During the last stage of GaAs NW growth no Ga is supplied, and so the remaining Ga in the droplet on top of the NWs is consumed, leading to an elongation of the NW at reduced diameter. In addition Fig. 1 illustrates the orientation of the $\{11\bar{1}\}$ shell facets with respect to the cores. A hexagonal prism symbolizing the GaAs NWs with $\langle 110 \rangle$ -oriented sidewalls is drawn schematically. In addition a tetrahedron depicting the equilibrium shape of Fe_3Si crystallites consisting of $\text{Fe}_3\text{Si}\{11\bar{1}\}$ planes is shown. The tilted $\text{Fe}_3\text{Si}\{11\bar{1}\}$ planes form extended shell facets. These facets are intersecting the top $\text{Fe}_3\text{Si}(111)$ plane, resulting in triangular features at the top which are visible in the SEM micrograph.

Figure 2 depicts the XRD curves of the $(\bar{2}20)$ reflection of GaAs/ Fe_3Si core/shell NWs, $T_S = 200^\circ\text{C}$. A radial $\omega/2\theta$ -scan (thick line) along the $[1\bar{1}0]$ direction and an angular ω -scan perpendicular to the $[1\bar{1}0]$ direction (thin line), together with their full widths at half maximum (FWHM) are given. The radial scan shows thickness fringes (marked by arrows) corresponding to a thickness of 14.3 nm equal to the Fe_3Si shell thickness (cf. Fig. 5(b)). The radial scan has a FWHM of 0.08° whereas the angular scan has a larger width of 0.55° . The FWHM in angular direction here corresponds to the range of twist of the NWs, as in-plane reflections are used.³⁵ The range of tilt of GaAs NWs was measured to be near $(0.28 \pm 0.1)^\circ$ using symmetrical out-of-plane measurements.

Figure 3 show XRD curves of GaAs/ Fe_3Si core/shell NWs, $T_S = 200^\circ\text{C}$. Radial $\omega/2\theta$ -scans along (a) the $\langle 110 \rangle$ and (b) the $\langle 211 \rangle$ directions are given. Scan (a) does not reveal any unexpected



Fe₃Si {111} Si terminated

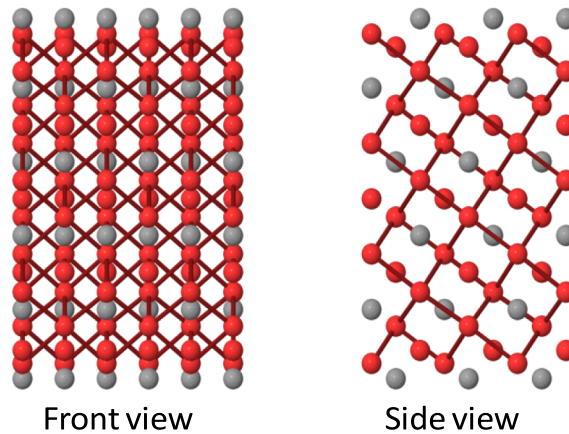


FIG. 6. Surface energy of differently terminated (term.) surfaces calculated by DFT in generalized gradient approximation. The structure of the Si-terminated Fe₃Si{111} surface is illustrated below, Fe atoms are symbolized as red balls whereas Si atoms as grey balls.

maxima due to polycrystalline material whereas scan (b) exhibits additional maxima caused by the wurtzite regions in the GaAs cores. Merely the (400) maximum points to another orientation of some of the crystallites probably caused by additional twins in the cores that are not parallel to the GaAs/Si interface. The detection of the wurtzite regions in the GaAs cores again points to the fact, that our measurements are sensitive for the core/shell NWs only.

Figure 4 demonstrates in-plane reciprocal space maps of the ($\bar{2}20$)-reflection of GaAs NWs (left) and GaAs/Fe₃Si core/shell NWs (center and right) grown by MBE on a Si(111) substrate. The growth temperatures of the Fe₃Si shells were 200 °C (center) and 300 °C (right). The crystallographic directions are sketched below. The radial direction ($\omega/2\theta$) of the scans is vertical and the angular direction (ω) horizontal. The facets of the pillar shaped cores with hexagonal cross section are clearly distinguished by streaks in the diffuse scattering pointing along the $\langle 110 \rangle$ directions. Remarkably, in the central map core streaks along the $\langle 110 \rangle$ directions are still visible although they are superimposed by additional streaks along the $\langle 1\bar{2}1 \rangle$ directions originating from the facets of the Fe₃Si shells. In the map shown on the right side only streaks of the shell facets remain. Additional

maxima above the main peak indicate chemical reactions between Fe₃Si and GaAs occurring at $T_S = 300$ °C near the interface similar as those observed for planar films on GaAs.^{9,36}

Figure 5 shows a multi-beam bright-field TEM micrograph, illustrating the orientations of the Fe₃Si facets of the core/shell NW on Si(111). In Fig. 5(a) the incident electron beam is oriented along $[\bar{1}\bar{1}0]$ in (b) along $[11\bar{2}]$. In (a) we observe facets of the Fe₃Si shell as tilted black linear contrast steps, in (b) we see smooth interfaces and surfaces. The roughening due to the faceting is not observed along this direction. The visibility of the thickness fringes in Fig. 2 points to the fact, that (1) we really measure the diffraction signal of the core/shell NWs only, and (2) that the thickness fringes are measured in an $(\omega/2\Theta)$ -scan along the $[1\bar{1}0]$ direction where the interfaces are smooth. A growth temperature of 200 °C results in this highly perfect Fe₃Si shell structure. The $(11\bar{1})$ surface nanofacets are expected to be inclined to the (110) cladding planes of the GaAs cores leading to an increase of the surface area A. There is a non negligible material transport over distances small compared to the NW lengths. On a larger length-scale the Fe₃Si shell is approximately reproducing the shape of the GaAs core NWs.²¹ The GaAs cores are usually not free of defects, especially near the Si/GaAs interface and during the late phase of GaAs NW growth planar defects connected to the transition from zincblende to wurtzite segments are found.³⁷ So the straight horizontal contrasts in the GaAs cores in Fig. 5(a) are caused by planar defects leading to alternating zincblende and wurtzite GaAs regions.

Figure 6 shows results of DFT calculations of surface energies of the Fe₃Si shells for a wide range of chemical potentials and several possible surface terminations. Fe₃Si surfaces were found to be Si-rich.^{38,39} In that case the Si-terminated Fe₃Si (111) planes are most favorable energetically, even if geometrical factors, i.e. the inclination angle between GaAs (110) and Fe₃Si (111) planes of $\psi = 35.3$ °, are taken into account. The (110) surface has an energy of $\gamma_{110} = 140$ meV·Å⁻². Hence the criterion for (111) facet formation is that the (111) surfaces have an energy less than $\gamma_{110} \cdot \cos(\psi) = 114.25$ meV·Å⁻². As a result our DFT calculations confirmed that the formation of facets reduces the overall surface energy.

V. CONCLUSIONS

GaAs core NWs were grown on the oxidized Si(111) surface inside holes of the SiO₂ film via the VLS growth mechanism. Then ferromagnetic Fe₃Si shells were grown resulting in continuous covering of the cores. A polycrystal film grew unintentionally between the NWs. We have successfully avoided the XRD signal of the polycrystal film by studying the ensemble of core/shell NWs using x-ray grazing incidence diffraction geometry. We did not observe additional orientations of the shell with respect to the core, i.e. the shells are pseudomorphic. Up to a growth temperature of 200 °C additional broadening of the shell diffraction maxima compared to those of the cores is rather limited. The analysis of the x-ray diffuse scattering revealed the hexagonal cross-section of the GaAs cores. In addition Fe₃Si nano-facets of the shells cause streaks rotated by an azimuthal angle of 30 °. The nano-facets consist e.g. of $\{111\}$ planes tilted around $\langle 011 \rangle$ axes towards the $\langle 211 \rangle$ direction, i.e. for $[111]$ oriented NWs the $(\bar{1}11)$ facets are most pronounced, forming a regular pattern along the GaAs NWs. The $\{111\}$ facets of Fe₃Si are formed because under our Si-rich conditions they have the lowest surface energy in agreement with the DFT calculations. We supported the hypothesis that the nanofaceted Fe₃Si shells found in the present work are a result of VW island growth.¹⁵ The role of the surface is more important for NWs than for planar films, the faceted growth of the lattice matched shells is an example for such surface related phenomena. Facetting will also play a role in systems with SK growth mode and strain-driven VW island growth.

ACKNOWLEDGEMENT

The authors thank Claudia Herrmann for her support during the MBE growth, Doreen Steffen for sample preparation, Astrid Pfeiffer for help in the laboratory, Anne-Kathrin Bluhm for the SEM micrographs, Esperanza Luna and Xiang Kong for valuable support and helpful discussion. We

thank the ESRF in Grenoble for providing beamtime during the experiment HC-1967. We thank Nathalie Boudet and Nils Blanc for their support during the beamtime. The beamtime for some preliminary measurements performed at the PHARAO U-125/2 KMC beamline of the storage ring BESSY II in Berlin is thankfully acknowledged as well. This work was supported in part by the Office of Naval Research through the Naval Research Laboratory's Basic Research Program. Some computations were performed at the DoD Major Shared Resource Center at AFRL.

- ¹ M. Hilse, Y. Takagaki, J. Herfort, M. Ramsteiner, C. Herrmann, S. Breuer, L. Geelhaar, and H. Riechert, *Appl. Phys. Lett.* **95**, 133126 (2009).
- ² A. Rudolph, M. Soda, M. Kiessling, T. Wojtowicz, D. Schuh, W. Wegscheider, J. Zweck, C. Back, and E. Reiger, *Nano Lett.* **9**, 3860 (2009).
- ³ D. Ruffer, R. Huber, and P. Berberich, *Nanoscale* **4**, 4989 (2012).
- ⁴ N. S. Dellas, J. Liang, B. J. Cooley, N. Samarth, and S. E. Mohny, *Appl. Phys. Lett.* **97**, 072505 (2010).
- ⁵ K. Tivakornasithorn, R. E. Pimpinella, V. Nguyen, X. Liu, M. Dobrowolska, and J. K. J. Furdyna, *J. Vac. Sci. Technol. B* **30**, 02115 (2012).
- ⁶ X. Yu, H. Wang, D. Pan, J. Zhao, J. Misuraca, S. Molnar, and P. Xiong, *Nano Lett.* **13**, 1572 (2013).
- ⁷ M. Hilse, J. Herfort, B. Jenichen, A. Trampert, M. Hanke, P. Schaaf, L. Geelhaar, and H. Riechert, *Nano Lett.* **13**, 6203 (2013).
- ⁸ B. Jenichen, M. Hilse, J. Herfort, and A. Trampert, *J. Cryst. Growth* **427**, 21 (2015).
- ⁹ J. Herfort, H.-P. Schönherr, and K. H. Ploog, *Appl. Phys. Lett.* **83**, 3912 (2003).
- ¹⁰ B. Jenichen, V. M. Kaganer, J. Herfort, D. K. Satapathy, H. P. Schönherr, W. Braun, and K. H. Ploog, *Phys. Rev. B* **72**, 075329 (2005).
- ¹¹ J. Herfort, H.-P. Schönherr, A. Kawaharazuka, M. Ramsteiner, and K. H. Ploog, *J. Cryst. Growth* **278**, 666 (2005).
- ¹² J. Herfort, B. Jenichen, V. Kaganer, A. Trampert, H. P. Schoenherr, and K. Ploog, *Physica E* **32**, 371 (2006).
- ¹³ J. Herfort, A. Trampert, and K. Ploog, *Int. J. Mater. Res.* **97**, 1026 (2006).
- ¹⁴ E. Bauer, *Z. Kristallographie* **110**, 372 (1958).
- ¹⁵ V. M. Kaganer, B. Jenichen, R. Shayduk, W. Braun, and H. Riechert, *Phys. Rev. Lett.* **102**, 016103 (2009).
- ¹⁶ C. Colombo, D. Spirkoska, M. Frimmer, G. Abstreiter, and A. FontcubertaiMorrall, *Phys. Rev. B* **77**, 155326 (2008).
- ¹⁷ N. Moll, A. Kley, E. Pehlke, and M. Scheffler, *Phys. Rev. B* **54**, 8844 (1996).
- ¹⁸ E. Uccelli, J. Arbiol, J. R. Morante, and A. F. i Morrall, *ACS Nano* **4**, 5985 (2010).
- ¹⁹ L. Pan, K. K. Lew, J. M. Redwing, and E. C. Dickey, *Nano Lett.* **5**, 1081 (2005).
- ²⁰ L. D. Marks, *Rep. Prog. Phys.* **57**, 603 (1994).
- ²¹ B. Jenichen, M. Hilse, J. Herfort, and A. Trampert, *J. Cryst. Growth* **410**, 1 (2015).
- ²² L. D. Landau and E. M. Lifshitz, *Statistical Physics*, 3rd ed. (Pergamon press, Oxford, 1980), p. 70.
- ²³ L. Vitos, A. V. Ruban, H. L. Skriver, and J. Kollar, *Surf. Sci.* **411**, 186 (1998).
- ²⁴ R. M. Martin, *Electronic Structure*, 1st ed. (Cambridge university press, Cambridge, 2004), p. 32.
- ²⁵ G. X. Qian, R. M. Martin, and D. J. Chadi, *Phys. Rev. B* **38**, 7649 (1988).
- ²⁶ P. Hohenberg and W. Kohn, *Phys. Rev.* **136**, B864 (1964).
- ²⁷ W. Kohn and L. J. Sham, *Phys. Rev.* **140**, A1133 (1965).
- ²⁸ W. Kohn, *Rev. Mod. Phys.* **71**, 1253 (1999).
- ²⁹ P. J. Hasnip, K. Refson, M. I. J. Probert, J. R. Yates, S. J. Clark, and C. J. Pickard, *Phil. Trans. R. Soc. A* **372**, 20130270 (2014).
- ³⁰ R. O. Jones, *Rev. Mod. Phys.* **87**, 897 (2015).
- ³¹ J. P. Perdew, K. Burke, and M. Ernzerhof, *Phys. Rev. Lett.* **77**, 3865 (1996).
- ³² G. Kresse and J. Furthmuller, *Phys. Rev. B* **54**, 11169 (1996).
- ³³ G. Kresse and J. Furthmuller, *Comput. Mater. Sci.* **6**, 15 (1996).
- ³⁴ H. Dosch, B. W. Batterman, and D. C. Wack, *Phys. Rev. Lett.* **56**, 1144 (1986).
- ³⁵ B. Jenichen, O. Brandt, C. Pfueller, P. Dogan, M. Knelangen, and A. Trampert, *Nanotechnology* **22**, 295714 (2011).
- ³⁶ C. Gusenbauer, T. Ashraf, J. Stangl, G. Hesser, T. Plach, A. Meingast, G. Kothleitner, and R. Koch, *Phys. Rev. B* **83**, 035319 (2011).
- ³⁷ P. Schroth, M. Kohl, J. W. Hornung, E. Dimakis, C. Somaschini, L. Geelhaar, A. Biermanns, S. Bauer, S. Lazarev, U. Pietsch, and T. Baumbach, *Phys. Rev. Lett.* **114**, 055504 (2015).
- ³⁸ U. Starke, J. Schardt, W. Weiss, W. Meier, C. Polop, P. L. de Andres, and K. Heinz, *Europhys. Lett.* **56**, 822 (2001).
- ³⁹ J. Hafner and D. Spisák, *Phys. Rev. B* **75**, 195411 (2007).